

Article

Effect of Force and Heat Coupling on Machined Surface Integrity and Fatigue Performance of Superalloy GH4169 Specimens

Xun Li ^{*}, Ruijie Gou  and Ning Zhang

School of Mechanical Engineering and Automation, Beihang University, Beijing 100191, China; sy2107405@buaa.edu.cn (R.G.); zhangnnin@buaa.edu.cn (N.Z.)

* Correspondence: lixun@buaa.edu.cn

Abstract: GH4169 is one of the key materials used to manufacture high-temperature load-bearing parts for aero-engines, and the surface integrity of these parts in service conditions significantly affects their high-temperature fatigue performance. Under a coupling effect of high temperature and alternating load, the evolution process of the machined surface integrity index of superalloy GH4169 specimens was studied, and fatigue performance tests at 20 °C, 450 °C, and 650 °C were carried out to analyze the primary factors affecting the high-temperature fatigue performance of specimens. The results indicated that the surface roughness of specimens remained essentially unchanged. However, the value of surface residual stress decreased significantly, with a release of more than 60% at the highest temperature. At 650 °C, the surface microhardness increased, while the degree of surface plastic deformation decreased under alternating loads. Simultaneously, when the surface roughness was less than R_a 0.4 μm , surface microhardness was the main factor affecting the high-temperature fatigue performance of specimens. The influence of surface microhardness on low-cycle fatigue performance was not consistent with that on high-cycle fatigue performance. The latter increased monotonically, whereas the former initially increased and then decreased with increasing surface microhardness.



Citation: Li, X.; Gou, R.; Zhang, N. Effect of Force and Heat Coupling on Machined Surface Integrity and Fatigue Performance of Superalloy GH4169 Specimens. *Metals* **2024**, *14*, 540. <https://doi.org/10.3390/met14050540>

Academic Editors: Matteo Benedetti and Giovanni Meneghetti

Received: 2 April 2024

Revised: 26 April 2024

Accepted: 30 April 2024

Published: 2 May 2024



Copyright: © 2024 by the authors. Licensee MDPI, Basel, Switzerland. This article is an open access article distributed under the terms and conditions of the Creative Commons Attribution (CC BY) license (<https://creativecommons.org/licenses/by/4.0/>).

Keywords: superalloy GH4169; high temperature; surface integrity; fatigue performance

1. Introduction

GH4169 is currently one of the most widely produced nickel-based superalloys. Its maximum service temperature can reach 650 °C; within this range, it can maintain its stable microstructure, exhibiting excellent mechanical properties, oxidation resistance, and corrosion resistance. Due to its exceptional characteristics, GH4169 has found widespread applications across various industries, particularly in the aerospace sector, where it is utilized for crafting essential hot-end load-bearing structural parts such as aero-engine turbine discs, integral blade discs, etc.

The environment in which aero-engines work is extremely harsh and requires superalloy parts to work stably under a variety of conditions, including high temperatures, complex stress, oxidation, and gas corrosion. Fatigue failure is identified as the primary cause of failure in key engine load-bearing parts, with most of the fatigue sources originating from the parts' surfaces. Consequently, improving the quality of surface machining can significantly enhance fatigue performance [1,2]. The evaluation of material surface machining quality is primarily based on surface integrity, which encompasses surface roughness, microcracks, work-hardening degree of the material surface layer, residual stress, and influence depth, as well as microstructure changes in the surface layer [3,4]. It is crucial to control and improve these factors for the anti-fatigue manufacturing of superalloys [5–7]. Numerous scholars have extensively researched this area. For example, Ulutan et al. [8] summarized the effects of various machining methods and process conditions on the surface integrity of superalloys. Thakur et al. [9] systematically concluded the research

status of surface integrity in superalloy machining; they identified the impact of different machining processes on surface work hardening, residual stress, and modified layers, and analyzed the influence of various surface integrity indexes on fatigue life. Wang et al. [10] analyzed the laws and mechanisms of surface roughness affecting the fatigue performance of superalloys and found that micro-defects caused by surface roughness produce stress, plastic strain, and damage concentration under fatigue load, which lead to fatigue crack initiation. As for surface work hardening and surface residual stress, most researchers suggested that moderate work hardening could inhibit the generation and expansion of fatigue cracks, which is beneficial to enhancing the fatigue life of parts [11,12], and surface residual compressive stress could effectively boost the fatigue performance of parts [13–16]. However, when parts are loaded, the surface residual stress would not remain stable and would release to some extent [17–19]. Jiang et al. [20] investigated the influence of changes in turning parameters on the microstructure of high-strength alloy steel. They found that a higher cutting speed can refine the grain of the material surface layer, increase the thickness of the surface strengthening layer, enhance the surface microhardness, and reduce the surface roughness of the specimen, thereby improving the fatigue performance of the material. Moreover, various studies have been conducted to assess the impact of alterations to processing conditions on the surface integrity and fatigue performance of materials [21–23].

Currently, numerous studies are being conducted to explore the influence of surface integrity on the fatigue performance of superalloy GH4169 under room temperature conditions. However, it is important to note that superalloy parts primarily operate under the coupling condition of mechanical force and heat. During the use of parts, each surface integrity index may not remain stable [24–26], and their trends of variation have not yet been clarified. To address this gap, the present study aimed to investigate the evolution process of the surface integrity indexes of superalloy GH4169 turned specimens under force and heat coupling. Additionally, a series of high-temperature fatigue performance tests were conducted to analyze the key factors affecting the fatigue performance of GH4169 at different temperatures. The insights gained from this study offer valuable guidance for the anti-fatigue manufacturing of GH4169 components under high-temperature service conditions, enhancing their overall reliability and durability.

2. Surface Integrity Measurement

2.1. Composition and Mechanical Properties of Materials

The experimental materials were superalloy GH4169 samples which had undergone solid solution and aging treatment. Tables 1 and 2 show the chemical composition and mechanical properties of the material at different temperatures.

Table 1. Chemical composition of GH4169 (wt.%).

C	Nb	Si	Mn	Cr	Ti	Al	Mo	Ni	Cu	Co	Fe
<0.08	4.75~5.5	<0.35	<0.35	17~20	0.75~1.15	0.3~0.7	2.8~3.3	50~55	0.3	<1.0	Bal.

Table 2. Mechanical properties of superalloy GH4169 at different temperatures.

Temperature /°C	Yield Strength σ_s/MPa	Tensile Strength σ_b/MPa
20	1140	1418
450	1030	1251
650	985	1129
750	781	808

2.2. Experiment Scheme

Figure 1 illustrates the structural form of the GH4169 specimens. The machined sections include the linear segment in the middle of the specimen and the partial arcuate

segments along its edges, which correspond to the areas traversed by the cutting tool as indicated in the figure. The relevant surface integrity metrics were measured at the machined linear segment of the specimen.

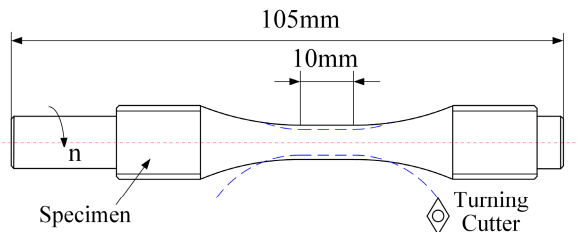


Figure 1. Machining diagram of superalloy GH4169 specimens.

The experiment used AlTiN-coated carbide turning tools with a front angle of 0° , a back angle of 7° , and a tool tip arc radius of 0.2 mm. According to the relevant research about the influence of turning parameters on surface integrity [27–29], the machining parameters were adopted as follows: $v_c = 20$ m/min, $f = 0.02$ mm/r, $a_p = 0.2$ mm. These parameters were chosen to control the machined surface roughness and cause an appropriate level of plastic deformation on the specimens' surfaces, enabling the analysis of the evolution process of the surface integrity indexes.

The experimental loading equipment was a high-frequency fatigue-testing machine, outfitted with a tubular furnace to complete high-temperature loading and fatigue testing. The fatigue-testing machine operated within a frequency range of 80–250 Hz, its maximum tensile load capacity was 100 kN, and the maximum alternating load was 50 kN.

For the high-temperature loading, the test temperatures were set to 20 °C, 450 °C, 650 °C, and 700 °C, respectively. The parameters of the alternating load were as follows: a loading frequency of 114 ± 1 Hz, a stress ratio r of 0.1, and a load waveform of a sine wave. In conjunction with Table 2, the maximum loads σ_{\max} were set to 770 MPa, 820 MPa, and 880 MPa, respectively. Based on these parameters, loading schemes were designed for each temperature condition, as detailed in Table 3.

Table 3. Load conditions for high-temperature loading.

No.	Temperature /°C	Maximum Load σ_{\max} /MPa	Number of Loading Cycles $N/\times 10^5$
1	20	820	1
2	450	820	1
3	650	High temperature Treatment (HT): $\sigma_{\max} = 0$	
4			1
5	650	770	5
6			20
7			1
8	650	820	5
9			20
10			1
11	650	880	5
12			20
13			0.1
14	700	820	1

To ensure the stability and reliability of the surface integrity measurements, each specimen group was tested 3~5 times. The test methods of surface integrity were conducted as follows:

Surface roughness was measured utilizing a contact roughness measuring instrument; a Vickers microhardness test was conducted to assess the surface microhardness; the surface residual stress of the specimens parallel to the load direction was gauged by an

X-ray stress meter; the microstructure of the specimens was observed with Focused Ion Beam (FIB)–Scanning Electron Microscopy (SEM).

2.3. Measurement Results and Evolution Process of Surface Integrity

2.3.1. Surface Roughness and Surface Morphology

Figure 2 demonstrates the impact of various test conditions on surface roughness. Initially, the turned specimens exhibited a surface roughness of R_a 0.32 μm and R_z 1.85 μm (represented by red and blue dashed lines respectively in Figure 2). At higher temperatures, the specimens' surfaces underwent oxidation, resulting in the formation of a random and incompletely uniform oxide layer, thereby altering the surface roughness. Under alternating loads, the surface layer of the specimens deformed, modifying the average height of the surface profile and, consequently, the surface roughness. However, the comparison of the surface roughness measurements of specimen No. 1 (solely subjected to loading) and specimen No. 3 (solely undergoing high-temperature treatment) in Table 3 reveals no significant changes in roughness values. Furthermore, as evident from the data presented in Figure 2, the high-temperature loading test did not significantly alter the R_a values or R_z values. This suggests that neither the combined effect of force and heat nor the isolated action of any single factor exerted a significant influence on the surface roughness of the specimens.

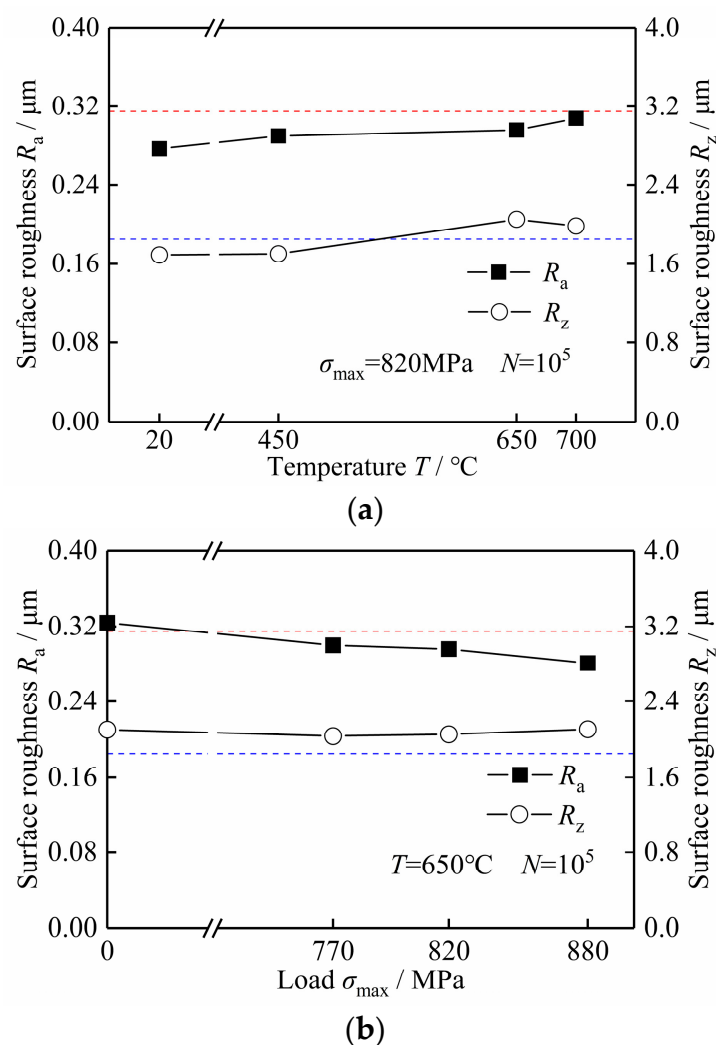


Figure 2. Cont.

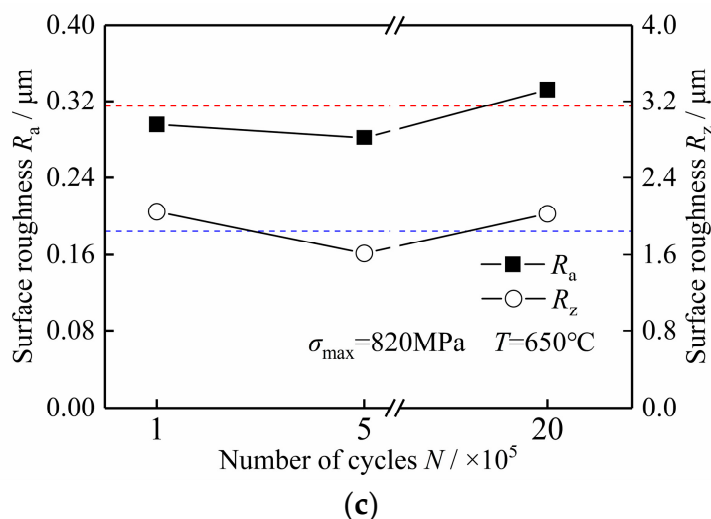


Figure 2. Effect of force and heat coupling on machined surface roughness of specimens. (a) Effect of temperature variation on surface roughness; (b) effect of load variation on surface roughness; (c) effect of the number of loading cycles on surface roughness.

Figure 3 shows the surface morphology of the specimens with various test conditions. Since the applied maximum load was less than the material's yield strength at both 20 °C and 450 °C, there was no obvious change in the surface morphology of group (a) or group (b). At 650 °C, an oxide layer formed on the specimens' surfaces, resembling those of high-temperature-treated samples. Overall, the surface turning texture of the specimens was still clearly visible, so their surface roughness remained at the original level.

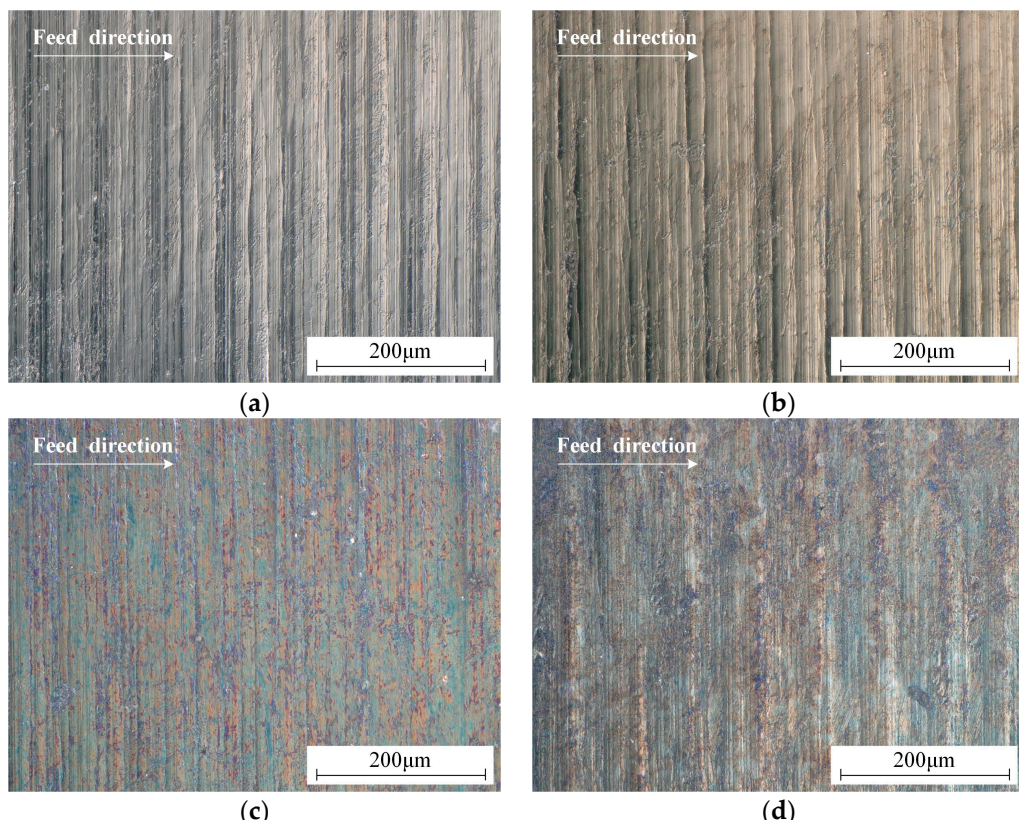


Figure 3. Surface morphology of specimens under different conditions: (a) $\sigma_{\max} = 820$ MPa, $N = 1 \times 10^5$, $T = 20$ °C; (b) $\sigma_{\max} = 820$ MPa, $N = 1 \times 10^5$, $T = 450$ °C; (c) $\sigma_{\max} = 770$ MPa, $N = 1 \times 10^5$, $T = 650$ °C; (d) $\sigma_{\max} = 820$ MPa, $N = 1 \times 10^5$, $T = 650$ °C.

2.3.2. Surface Residual Stress

The impact of temperature change on the surface residual stress with the coupling effect of force and heat is shown in Figures 4 and 5. The surface residual stress of the turned specimens measured approximately -588 MPa. When the maximum test load σ_{\max} remained constant, an increase in temperature led to a heightened degree of residual stress relief. Notably, at 650 °C, the release degree exceeded 50% , whereas under sole high-temperature treatment or cyclic loading conditions, it was 18% and 20.8% (as shown in Figure 5), respectively. As the test temperature escalated to 700 °C, the mechanical properties of the specimens decreased noticeably, resulting in a substantial reduction in surface residual stress to -156.4 MPa after 1×10^4 cycles of loading.

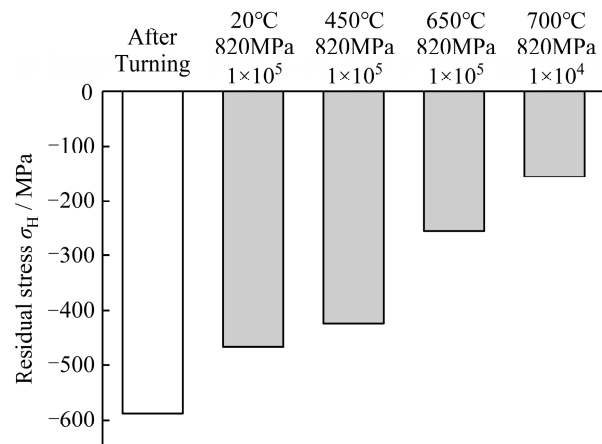


Figure 4. Effect of temperature change on residual stress release of specimens.

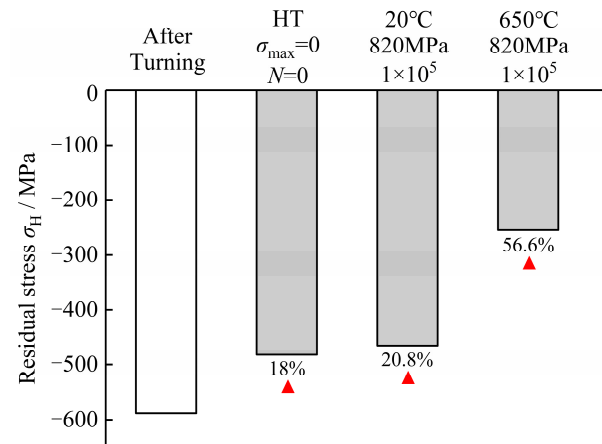


Figure 5. Release degree of surface residual stress under different conditions.

Figure 6 illustrates the influence of varying loading conditions on surface residual stress. Regardless of specimen groups, the surface residual stress remained relatively constant at approximately -200 MPa upon release. Furthermore, a higher load led to a faster attainment of a stable surface residual stress value. When σ_{\max} reached 880 MPa, specimens fractured after cyclic loading up to 5.89×10^5 times. The stable surface residual stress prior to fracture was comparable to that observed for specimens at σ_{\max} values of 770 MPa and 820 MPa. This observation suggests that an increase in load primarily influenced the rate of residual stress release, rather than its overall degree of release.

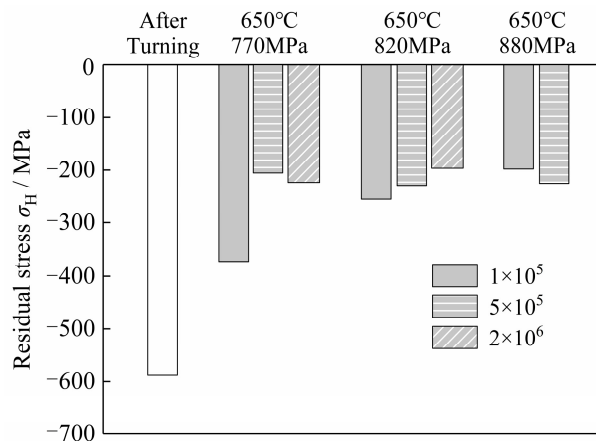


Figure 6. Effect of load and the number of loading cycles on residual stress release.

The test also adopted new parameters to turn specimens ($v_c = 15 \text{ m/min}$, $f = 0.01 \text{ mm/r}$, $a_p = 0.4 \text{ mm}$) and analyzed the trends in residual stress release under the conditions of $\sigma_{\max} = 820 \text{ MPa}$ and $T = 650 \text{ }^\circ\text{C}$. The results are shown in Figure 7. After 1×10^5 loading cycles, GH4169 specimens machined with the original parameters exhibited a stable level of surface residual stress (approximately -200 MPa). Specimens machined with the new parameters exhibited a large degree of surface plastic deformation, and their surface residual stress stabilized at about -286 MPa after 5×10^5 loading cycles. The difference in residual stress among specimens exhibiting varying degrees of surface plastic deformation diminished following high-temperature loading, and the overall level was low, which would obviously weaken the influence of residual stress on the high-temperature fatigue performance of specimens.

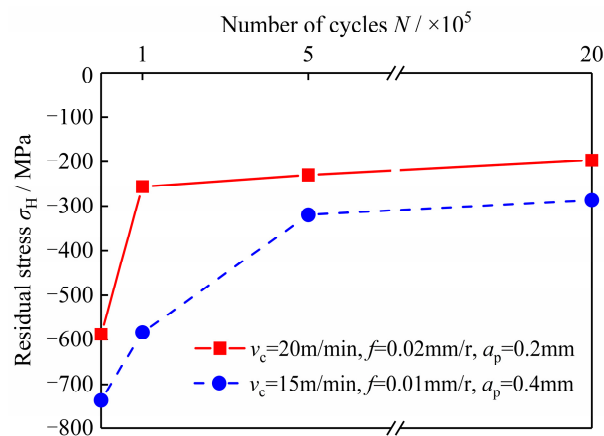


Figure 7. Variation trends of surface residual stress with different turning parameters ($650 \text{ }^\circ\text{C}$, 820 MPa).

2.3.3. Surface Microhardness

Figure 8 depicts the evolution process of surface microhardness. The hardness of the GH4169 matrix after the solid solution and aging treatment was about 432 HV, which is indicated by red dashed lines in the figure, and this increased to around 516 HV through turning. As the temperature escalated, a gradual increase in surface microhardness was observed, particularly at temperatures ranging from $650 \text{ }^\circ\text{C}$ to $700 \text{ }^\circ\text{C}$, where it rose to 540–550 HV, resulting in a surface hardening rate exceeding 25%. In addition, alternating load was shown to reduce the degree of surface plastic deformation. When the load and the number of loading cycles grew, the surface microhardness of specimens would decrease, but this effect was weak. Under the coupling effect of force and heat, the change in surface microhardness was mainly affected by temperature.

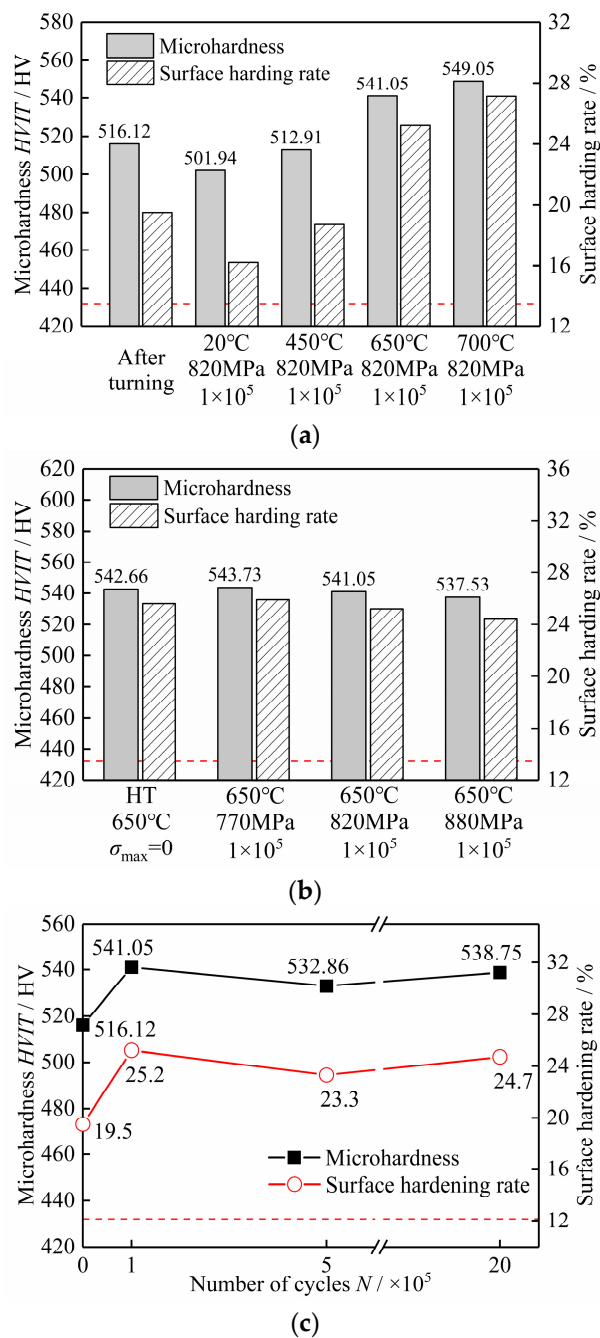


Figure 8. Effect of force and heat coupling on surface microhardness. (a) Effect of temperature variation on surface microhardness; (b) effect of load variation on surface microhardness; (c) effect of the number of load cycles on surface microhardness (650 °C, 820 MPa).

2.3.4. Surface Layer Microstructure

Figure 9 illustrates the changes in the surface layer microstructure of the specimens; with the rise in σ_{\max} , the degree of plastic deformation in the specimens' surface layers declined. Simultaneously, an elevation in temperature gave rise to compositional alterations within the microstructure of the specimens: at 650 °C, significant precipitates were observed at the grain boundary of the specimens. GH4169 is mainly composed of matrix phase γ , strengthening phase γ'' , auxiliary strengthening phase γ' , equilibrium phase δ , carbide, etc. In high-temperature environments, particularly at the extreme operating temperature in this case, strengthening phase γ'' was easy to aggregate and grow. It transformed to equilibrium phase δ , and precipitated at the grain boundary, which could strengthen the

grain boundary, hinder grain boundary slip and crack propagation, and simultaneously elevate the hardness of the material to a certain extent. However, excessive precipitation of the δ phase led to a decrease in the strengthening phase and sharply declined the mechanical properties of the material. Moreover, as the δ phase belongs to the brittle phase, it increased the brittleness of the material, further reducing the plastic deformation capacity of the surface layer.

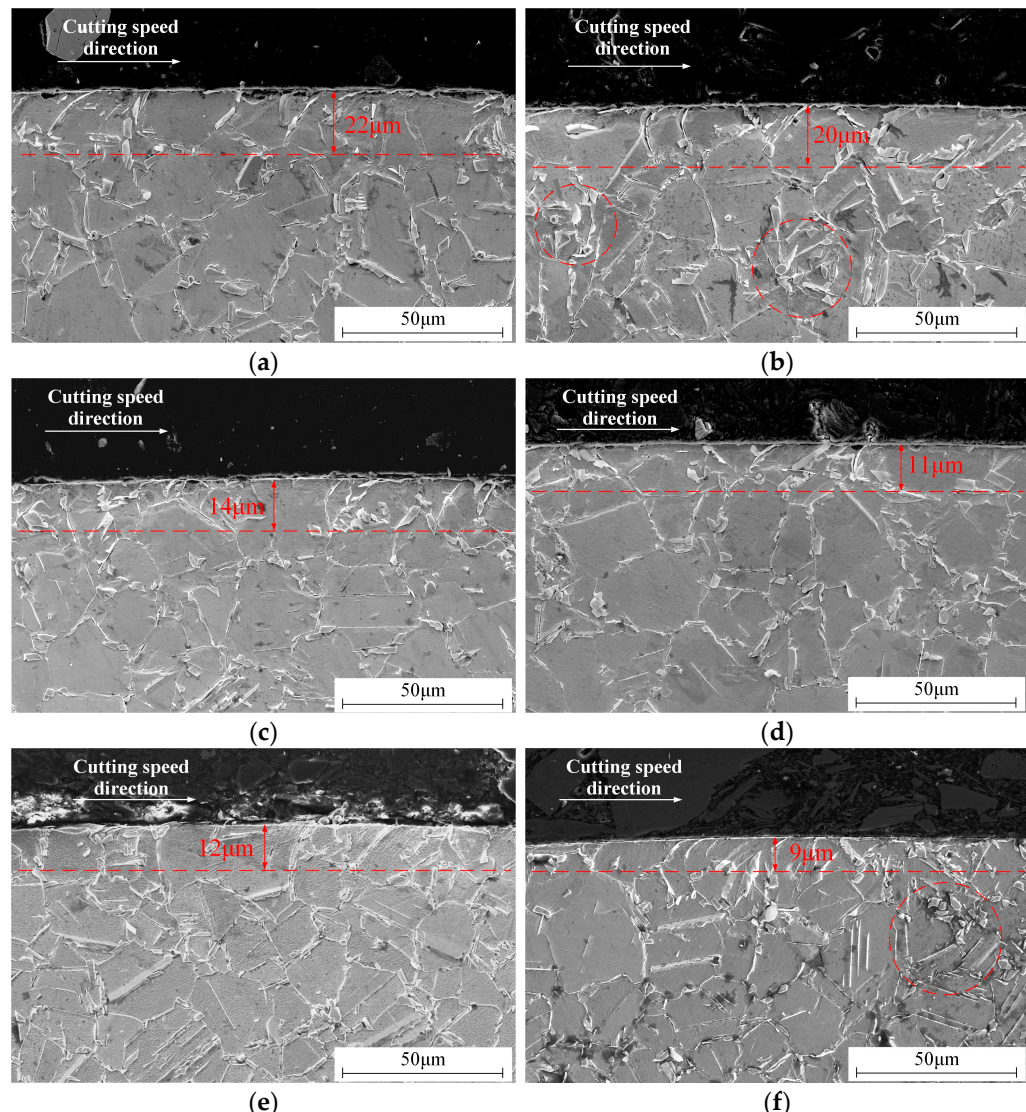


Figure 9. Surface layer microstructure of specimens with different test conditions: (a) after turning; (b) HT ($\sigma_{\max} = 0$); (c) $T = 20\text{ }^{\circ}\text{C}$, $\sigma_{\max} = 820\text{ MPa}$, $N = 1 \times 10^5$; (d) $T = 450\text{ }^{\circ}\text{C}$, $\sigma_{\max} = 820\text{ MPa}$, $N = 1 \times 10^5$; (e) $T = 650\text{ }^{\circ}\text{C}$, $\sigma_{\max} = 820\text{ MPa}$, $N = 1 \times 10^5$; (f) $T = 650\text{ }^{\circ}\text{C}$, $\sigma_{\max} = 880\text{ MPa}$, $N = 1 \times 10^5$.

3. GH4169 High-Temperature Fatigue Performance Tests

3.1. Experimental Plan

When subjected to the coupling effect of force and heat, the machined surface roughness of the GH4169 specimens remained essentially unchanged. Assuming that surface roughness was controlled at a lower level, the high-temperature fatigue performance of the specimens was mainly affected by the degree of surface plastic deformation, which is related to surface residual stress, surface work hardening, and microstructure changes in the surface layer. Combined with these research results, high-temperature fatigue tests were conducted. It was necessary to minimize the effect of surface roughness and control

the feed rate f at a lower level, and the surface plastic deformation degree of the specimens was adjusted by changing the cutting speed v_s and the cutting depth a_p .

According to the mechanical properties of the GH4169 alloy at different temperatures, the conditions of the fatigue performance tests were set as follows: $\sigma_{\max} = 1040$ MPa and $T = 20^\circ\text{C}$, $\sigma_{\max} = 930$ MPa and $T = 450^\circ\text{C}$, $\sigma_{\max} = 880$ MPa and $T = 650^\circ\text{C}$. The other loading conditions remained unchanged. Each parameter group was tested 3~5 times, and the average values were taken as the final results.

3.2. Fatigue Performance Test Results and Discussion

The machining parameters, surface integrity indexes, and fatigue life at different temperatures of each group of specimens are shown in Table 4. It is worth noting that, to ensure the accuracy of the study, the results of each group were obtained as the average of five separate experiments.

Table 4. Fatigue test results at different temperatures (mean values of 5 tests).

Cutting Speed v_s (m·min ⁻¹)	Feed Rate f (mm·r ⁻¹)	Cutting Depth a_p (mm)	Surface Roughness		Surface Microhardness HVIT (HV)	Surface Residual Stress σ_H (MPa)	Fatigue Life N_f ($\times 10^5$)		
			R_a (μm)	R_z (μm)			650 °C 1040 MPa	450 °C 930 MPa	20 °C 880 MPa
15	0.01	0.4	0.35	2.23	544.07	-735.5	3.98	6.76	7.53
15	0.01	0.3	0.34	1.99	529.26	-621.8	4.24	7.13	7.84
20	0.02	0.2	0.32	1.85	516.12	-588.1	5.89	6.52	7.76
25	0.02	0.1	0.3	1.83	510.7	-550.2	6.74	6.07	--
25	0.04	0.1	0.36	2.17	503.71	-555.7	5.88	5.51	6.8
30	0.06	0.1	0.39	2.40	489.43	-583	4.91	5.46	6.15

The fatigue fracture of specimens arises from cyclic plastic strain in areas of stress or strain concentration. Although the applied test load is below the yield strength of the materials, stress concentration phenomena still occur in local regions. Firstly, irregular grooves formed on the machined surface of specimens lead to stress concentration, resulting in plastic deformation and generating irreversible tensile strains in partial positions. Secondly, material imperfections and different grain orientations in the loading direction cause some grains to yield and produce plastic deformation, even though specimens as a whole are in the state of elastic deformation. The combined effect of these two factors creates localized strain concentration zones on the specimen surface which are highly susceptible to microcrack formation under alternating loads, ultimately leading to fatigue failure.

In the tests, GH4169 specimens were machined with a smaller feed, and the impact of surface morphology on fatigue performance was minimal. In the study of the evolution process of the surface integrity index, surface residual stress was released to a lower level after high-temperature loading, leading to a significant reduction in its influence on fatigue performance. Consequently, at elevated temperatures, the fatigue performance of the specimens was primarily influenced by surface microhardness. As Figure 10 illustrates, the fatigue life of the specimens displayed a trend of increasing and then decreasing with an increase in surface microhardness.

The loading situation was analyzed, as shown in Figure 11, and it was observed that the mechanical properties of the grains in the surface layer were improved after plastic deformation. This resulted in surface work hardening, surface residual compressive stress, and grain refinement, which effectively suppressed microcrack formation and thereby improved the fatigue performance of the specimens [30,31]. Macroscopically, when the maximum load σ_{\max} was less than the yield strength σ_s , the whole specimen remained in an elastic deformation state and the total deformation amounts of the surface layer material and the internal matrix material were identical. But from a microscopic point of view, due to the presence of micromorphology, the deformation at each position of the surface was uneven, and the actual strain ϵ_1 of the grains in the strain concentration region was large, even entering a plastic deformation state. If the plastic deformation degree became

excessive, the deformable amount of surface layer grains would be greatly reduced when they entered the plastic deformation again, and the actual strain amount of some grains might exceed their limit strain amount, i.e., $\varepsilon_1 > \varepsilon_b'$, causing the grains to fracture during the initial loading stage and form microcracks. The fatigue performance of the specimens would greatly decrease [32,33].

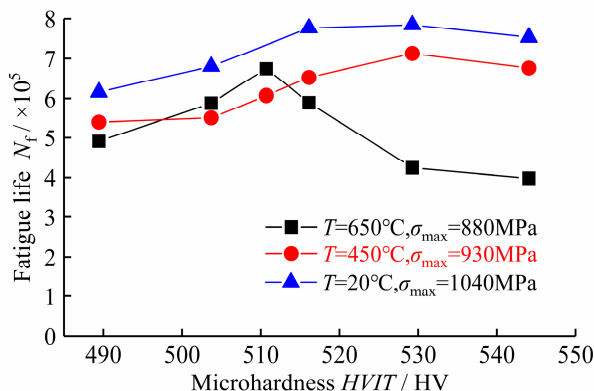


Figure 10. Influence of machined surface microhardness on specimens' fatigue performance.

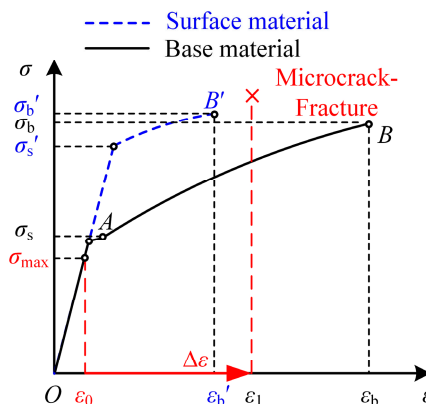


Figure 11. The mechanism of micro cracks on the surface of specimens.

It is worth noting that the surface microhardness corresponding to the maximum fatigue life of the specimens was about 510 HV at $T = 650^\circ\text{C}$ and $\sigma_{\max} = 880\text{ MPa}$, while it was 530 HV at the other two temperatures. This disparity is attributed to a compositional alteration within the materials at the limit service temperature. Specifically, a significant proportion of strengthened phase γ'' transformed into equilibrium phase δ and precipitated at the grain boundary, which resulted in an overall microhardness enhancement. However, this transformation also led to an increase in the brittleness of the surface layer material, and its plastic deformation ability was further reduced. During the loading stage, in circumstances of moderate or even minor plastic deformation, the strain of grains located in strain concentration areas may potentially exceed their ultimate strain limits, thereby increasing the probability of fatigue crack formation on the surface of the specimens. Therefore, the alteration in surface microhardness exerted a more pronounced influence on the fatigue behavior of the specimens at 650°C .

The high-cycle fatigue performance test was conducted at $T = 650^\circ\text{C}$ and $\sigma_{\max} = 820\text{ MPa}$. The other test conditions were kept constant. The influence of microhardness on the fatigue life of the specimens is shown in Figure 12. The results indicate that within the range of the test parameters, varying degrees of work hardening were all beneficial in enhancing the high-cycle fatigue life of the specimens. This was because at lower test loads, the actual strains of the grains were small, and the degree of strain concentration of the surface layer microstructure decreased. Even after producing large surface plastic deformation by turning, ε_1 was still

less than $\varepsilon b'$. Therefore, under high-cycle fatigue conditions, a large degree of surface plastic deformation was still advantageous in improving the fatigue performance of the specimens.

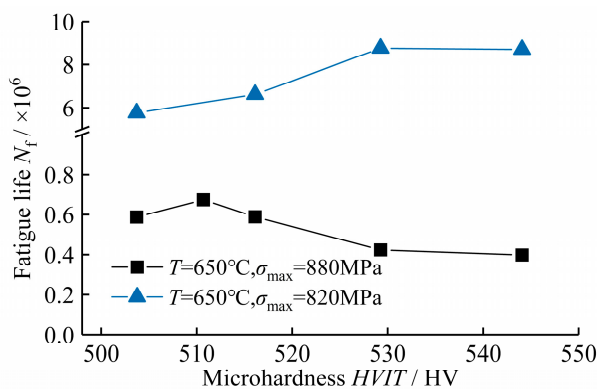


Figure 12. The effect of surface microhardness on the high-cycle and low-cycle fatigue of the specimens.

The fatigue fracture morphology of the high-cycle and low-cycle fatigue specimens was observed, and the results are presented in Figure 13, the initiation of fatigue fracture has been marked with a red dashed circle. It can be observed that the fatigue fractures of the low-cycle fatigue specimens initiated either from the surface or from the subsurface regions located approximately 40~80 μm from the surface. This failure mode is prevalent in the majority of aerospace components, and similar phenomena have been reported in numerous studies [34]. In contrast, during the high-cycle fatigue tests, surface work hardening significantly strengthened the surface of the specimens. Consequently, the locations of fatigue fracture initiation shifted towards the interior of the specimens, with a distance exceeding 200 μm from the surface. This hindered the formation of fatigue cracks on the surface, thereby enhancing the fatigue life of the specimens.

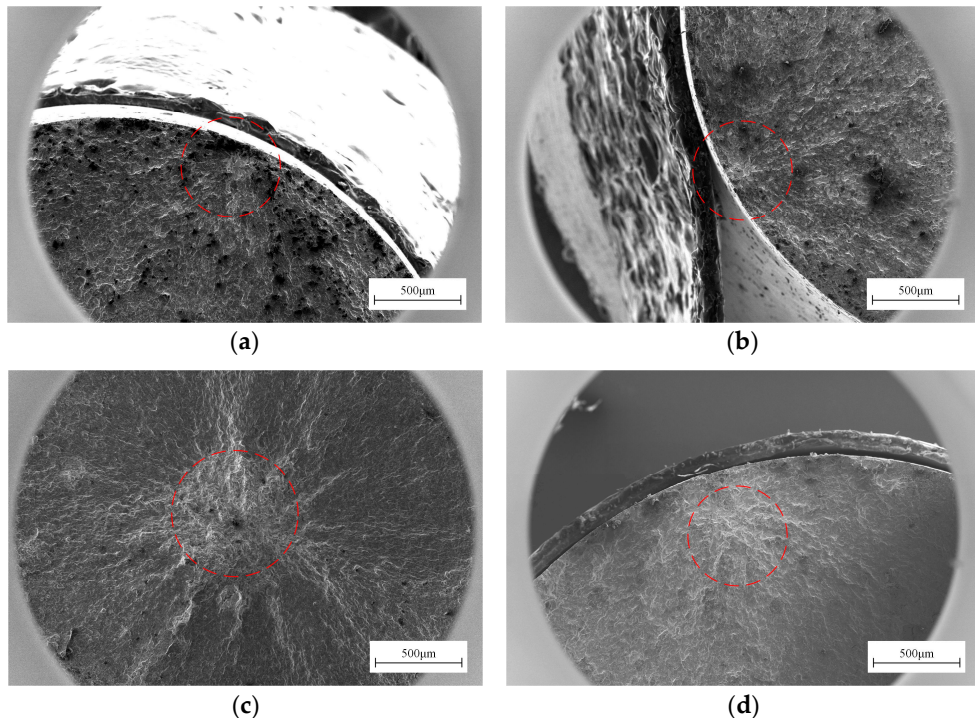


Figure 13. Fatigue fracture morphology of specimens with different levels of surface microhardness: (a) 510.70 HV, $\sigma_{\max} = 880\text{ MPa}$, $N_f = 6.74 \times 10^5$; (b) 544.07 HV, $\sigma_{\max} = 880\text{ MPa}$, $N_f = 3.98 \times 10^5$; (c) 529.26 HV, $\sigma_{\max} = 820\text{ MPa}$, $N_f = 8.75 \times 10^6$; (d) 544.07 HV, $\sigma_{\max} = 820\text{ MPa}$, $N_f = 8.69 \times 10^6$.

4. Conclusions

- (1) Compared to room-temperature conditions, the residual stress on the machined surface of GH4169 specimens undergoes a more significant release under the coupling effect of force and heat. As the test temperature rises, the extent of release also escalates. At 650 °C, in diverse conditions, the degree of surface residual stress release in all groups of specimens ultimately exceeded 60%. Concurrently, an increase in the maximum load σ_{\max} leads to an accelerated rate of residual stress release.
- (2) Alternating loading mitigates the extent of plastic deformation on the machined surface of specimens, resulting in a downward trend in surface microhardness as σ_{\max} increases. However, at elevated temperatures, the strengthening phase γ'' within the microstructure of GH4169 transforms into the equilibrium phase δ . This precipitation of the δ phase enhances the microhardness of specimens. As the temperature rises, this phenomenon becomes more pronounced; specifically, at 650 °C, the surface microhardness of the machined specimens increased from 516.12 HV to a range of 530–545 HV.
- (3) The fatigue performance of GH4169 specimens at high temperatures is primarily influenced by surface microhardness, provided that the machined surface roughness remains below R_a 0.4 μm . Under low-cycle fatigue conditions, the fatigue life of specimens exhibits an initial increase followed by a decrease as the surface microhardness increases. Compared with 20 °C and 450 °C, the fatigue life of specimens at 650 °C is more significantly affected by variations in surface microhardness. Conversely, in high-cycle fatigue, the degree of surface strain concentration decreases, and under the given experimental conditions, larger surface microhardness and surface plastic deformation remain advantageous for enhancing the high-temperature fatigue performance of specimens.

The aforementioned conclusions carry significant implications for the anti-fatigue manufacturing of the superalloy GH4169. They serve as valuable references for controlling the surface integrity of machined aerospace components and also guiding the selection of appropriate machining parameters and process conditions. Furthermore, during the manufacturing process, it is crucial to take into account the actual operating conditions of various parts and purposefully manage their surface integrity indicators. This ensures that the performance requirements of the components are satisfied while simultaneously extending their service life.

Author Contributions: Conceptualization, X.L. and R.G.; Investigation, R.G. and N.Z.; Methodology, X.L. and R.G.; Supervision, X.L.; Visualization, R.G. and N.Z.; Writing—original draft, R.G.; Writing—review and editing, X.L. and R.G. All authors have read and agreed to the published version of the manuscript.

Funding: This research was funded by “National Natural Science Foundation of China, grant number 51875028”.

Data Availability Statement: All experimental data are presented within the manuscript.

Conflicts of Interest: The author declares no conflicts of interest.

References

1. Hardy, M.C.; Herbert, C.R.J.; Kwong, J.; Li, W.; Axinte, D.A.; Sharman, A.R.C.; Encinas-Oropesa, A.; Withers, P.J. Characterising the integrity of machined surfaces in a powder nickel alloy used in aircraft engines. *Procedia CIRP* **2014**, *13*, 411–416. [[CrossRef](#)]
2. Bons, J.P. A review of surface roughness effects in gas turbines. *J. Turbomach.* **2010**, *132*, 021004-1–021004-16. [[CrossRef](#)]
3. Field, M.; Kahles, J.F. The surface integrity of machined-and ground high-strength steels. *DMIC Rep.* **1964**, *210*, 54–77.
4. Liu, J.; Chen, G.; Zhao, L.; Yu, Z.; Jia, X. Research status and development trend of cutting surface integrity of aerospace alloy materials. *Int. J. Adv. Manuf. Technol.* **2023**, *127*, 45–63. [[CrossRef](#)]
5. Yao, J.; Li, X.; Du, B.; Zhang, N.; Gou, R. Research status of influence mechanism of surface integrity on fatigue behavior of metal workpieces: A review. *Int. J. Adv. Manuf. Technol.* **2024**, *131*, 3401–3419. [[CrossRef](#)]

6. Mustafa, G.; Li, B.; Zhang, S. Cutting condition effects on microstructure and mechanical characteristics of Ni-based superalloys—A review. *Int. J. Adv. Manuf. Technol.* **2024**, *130*, 3179–3209. [[CrossRef](#)]
7. Liao, Z.; Monaca, A.L.; Murray, J.; Speidel, A.; Ushmaev, D.; Clare, A.; Axinte, D.; M’Saoubi, R. Surface integrity in metal machining—Part I: Fundamentals of surface characteristics and formation mechanisms. *Int. J. Mach. Tools Manuf.* **2021**, *162*, 103687. [[CrossRef](#)]
8. Ulutan, D.; Ozel, T. Machining induced surface integrity in titanium and nickel alloys: A review. *Int. J. Mach. Tools Manuf.* **2011**, *51*, 250–280. [[CrossRef](#)]
9. Thakur, A.; Gangopadhyay, S. State-of-the-art in surface integrity in machining of nickel-based super alloys. *Int. J. Mach. Tools Manuf.* **2016**, *100*, 25–54. [[CrossRef](#)]
10. Wang, J.J.; Wen, Z.W.; Zhang, X.H.; Zhao, Y.C.; Yue, Z.F. Effect mechanism and equivalent model of surface roughness on fatigue behavior of nickel-based single crystal superalloy. *Int. J. Fatigue* **2019**, *125*, 101–111. [[CrossRef](#)]
11. Xie, L.; Palmer, D.; Otto, F.; Wang, Z.; Wang, Q.J. Effect of surface hardening technique and case depth on rolling contact fatigue behavior of alloy steels. *Tribol. Trans.* **2015**, *58*, 215–224. [[CrossRef](#)]
12. Sealy, M.P.; Guo, Y.B.; Caslaru, R.C.; Sharkins, J.; Feldman, D. Fatigue performance of biodegradable magnesium–calcium alloy processed by laser shock peening for orthopedic implants. *Int. J. Fatigue* **2016**, *82*, 428–436. [[CrossRef](#)]
13. Pramanik, A.; Dixit, A.R.; Chattopadhyaya, S.; Uddin, M.S.; Dong, Y.; Basak, A.K.; Littlefair, G. Fatigue life of machined components. *Adv. Manuf.* **2017**, *5*, 59–76. [[CrossRef](#)]
14. Wang, P.; He, Z.; Zhang, Y.; Zhang, S. Control of grinding surface residual stress of Inconel 718. *Procedia Eng.* **2017**, *174*, 504–511. [[CrossRef](#)]
15. Chen, H.; Liu, Z.; Wang, X.; Wang, Y.; Liu, S. Effect of surface integrity on fatigue life of 2024 aluminum alloy subjected to turning. *J. Manuf. Process.* **2022**, *83*, 650–666. [[CrossRef](#)]
16. Chin, K.S.; Idapalapati, S.; Ardi, D.T. Fatigue of surface-treated nickel-based superalloy at high temperature. *J. Mater. Eng. Perform.* **2019**, *28*, 7181–7187. [[CrossRef](#)]
17. Klotz, T.; Delbergue, D.; Bocher, P.; Lévesque, M.; Brochu, M. Surface characteristics and fatigue behavior of shot peened Inconel 718. *Int. J. Fatigue* **2018**, *110*, 10–21. [[CrossRef](#)]
18. Liao, Z.; Xu, D.; Luna, G.G.; Axinte, D.; Augustinavicius, G.; Sarasua, A.J.; Wretland, A. Influence of surface integrity induced by multiple machining processes upon the fatigue performance of a nickel based superalloy. *J. Mater. Process. Technol.* **2021**, *298*, 117313. [[CrossRef](#)]
19. Liu, G.; Huang, C.; Zhao, B.; Wang, W.; Sun, S. Effect of Machined Surface Integrity on Fatigue Performance of Metal Workpiece: A Review. *Chin. J. Mech. Eng.* **2021**, *34*, 118. [[CrossRef](#)]
20. Jiang, H.; Wang, C.; Ren, Z.; Yi, Y.; He, L.; Zhao, X. Influence of cutting velocity on gradient microstructure of machined surface during turning of high-strength alloy steel. *Mater. Sci. Eng. A* **2021**, *819*, 141354. [[CrossRef](#)]
21. Cui, P.; Liu, Z.; Zhao, J.; Ren, X. Correlation between Surface Integrity and Low Cycle Fatigue Life of Machined Inconel 718. *Metals* **2024**, *14*, 178. [[CrossRef](#)]
22. Sarikaya, M.; Gupta, M.K.; Tomaz, I.; Pimenov, D.Y.; Kuntoğlu, M.; Khanna, N.; Yıldırım, Ç.V.; Krolczyk, G.M. A state-of-the-art review on tool wear and surface integrity characteristics in machining of superalloys. *CIRP J. Manuf. Sci. Tech.* **2021**, *35*, 624–658. [[CrossRef](#)]
23. Wang, B.; Liu, Z.; Cai, Y.; Luo, X.; Ma, H.; Song, Q.; Xiong, Z. Advancements in material removal mechanism and surface integrity of high speed metal cutting: A review. *Int. J. Mach. Tools Manuf.* **2021**, *166*, 103744. [[CrossRef](#)]
24. Gill, C.M.; Fox, N.; Withers, P.J. Shakedown of deep cold rolling residual stresses in titanium alloys. *J. Phys. D Appl. Phys.* **2008**, *41*, 174005. [[CrossRef](#)]
25. Nikitin, I.; Besel, M. Residual stress relaxation of deep-rolled austenitic steel. *Scr. Mater.* **2008**, *58*, 239–242. [[CrossRef](#)]
26. Altenberger, I.; Nalla, R.K.; Sano, Y.; Wagner, L.; Ritchie, R.O. On the effect of deep-rolling and laser-peening on the stress-controlled low- and high-cycle fatigue behavior of Ti–6Al–4V at elevated temperatures up to 550 °C. *Int. J. Fatigue* **2012**, *44*, 292–302. [[CrossRef](#)]
27. Thakur, D.G.; Ramamoorthy, B.; Vijayaraghavan, L. Study on the machinability characteristics of superalloy Inconel 718 during high speed turning. *Mater. Des.* **2009**, *30*, 1718–1725. [[CrossRef](#)]
28. Amini, S.; Fatemi, M.H.; Atefi, R. High speed turning of Inconel 718 using ceramic and carbide cutting tools. *Arab. J. Sci. Eng.* **2014**, *39*, 2323–2330. [[CrossRef](#)]
29. Sun, J.; Wang, T.; Su, A.; Chen, W. Surface integrity and its influence on fatigue life when turning nickel alloy GH4169. *Procedia CIRP* **2018**, *71*, 478–483. [[CrossRef](#)]
30. Ren, N.F.; Yang, H.M.; Yuan, S.Q.; Wang, Y.; Tang, S.X.; Zheng, L.M.; Ren, X.D.; Dai, F.Z. High temperature mechanical properties and surface fatigue behavior improving of steel alloy via laser shock peening. *Mater. Des.* **2014**, *53*, 452–456. [[CrossRef](#)]
31. Zhao, X.; Xue, G.; Liu, Y. Gradient crystalline structure induced by ultrasonic impacting and rolling and its effect on fatigue behavior of TC11 titanium alloy. *Results Phys.* **2017**, *7*, 1845–1851. [[CrossRef](#)]
32. Li, X.; Guo, Z.; Yang, S.; Zhang, H.; Wang, Z. Study on the effect of milling surface plastic deformation on fatigue performance of 20Cr and TC17 specimens. *Metals* **2022**, *12*, 736. [[CrossRef](#)]

33. Suraratchai, M.; Limido, J.; Mabru, C.; Chieragatti, R. Modelling the influence of machined surface roughness on the fatigue life of aluminium alloy. *Int. J. Fatigue* **2008**, *30*, 2119–2126. [[CrossRef](#)]
34. Barter, S.A.; Molent, L.; Wanhill, R.J.H. Typical fatigue-initiating discontinuities in metallic aircraft structures. *Int. J. Fatigue* **2012**, *41*, 11–22. [[CrossRef](#)]

Disclaimer/Publisher's Note: The statements, opinions and data contained in all publications are solely those of the individual author(s) and contributor(s) and not of MDPI and/or the editor(s). MDPI and/or the editor(s) disclaim responsibility for any injury to people or property resulting from any ideas, methods, instructions or products referred to in the content.